RSC Advances

PAPER

View Article Online
View Journal | View Issue

Cite this: *RSC Adv.*, 2025, **15**, 17255

NIR-responsive cisplatin nanoparticles for synergistic chemo-photothermal therapy of oral squamous cell carcinoma†

Danrui Liu, Wenquan Wang, Yongjun Li, Suai Lin, Qingkun Jiang, Ruiyang Zou and Jiaxuan Qiu *

The typically occurring malignant tumor in the head and neck is oral squamous cell carcinoma (OSCC), which is highly aggressive and invasive. Despite surgical advancements, radiation, and chemotherapy, the prognosis for OSCC is still poor. Chemotherapy's effectiveness is frequently restricted by its serious side effects and the development of resistance. In this study, a cisplatin (CDDP)-loaded magnetic targeting nanoplatform (CDDP@PPy@Fe_3O_4) has been designed for synergistic chemo-photothermal therapy. PPy with carboxyl groups was first prepared by chemical oxidative polymerization. Then, Fe_3O_4 nanoparticles were synthesized *in situ* on its surface and loaded with CDDP through a reaction with the carboxyl groups. The CDDP@PPy@Fe_3O_4 nanocomposite serves not only as a nanocarrier for the targeted delivery of CDDP to alleviate the systemic toxicity of chemotherapy but also possesses excellent photothermal conversion properties, generating localized heat upon near-infrared laser irradiation that enables photothermal therapy. Contrary to using only chemotherapy or photothermal therapy, CDDP@PPy@Fe_3O_4 nanoparticles combined with NIR exposure exert superior anticancer effects against OSCC both *in vivo* and *in vitro* while exhibiting minimal side effects. Therefore, CDDP@PPy@Fe_3O_4 nanoparticles could be a promising candidate for nanomedicine in OSCC combination therapy.

Received 17th March 2025
Accepted 12th May 2025

DOI: 10.1039/d5ra01910a

rsc.li/rsc-advances

1. Introduction

Oral squamous cell carcinoma (OSCC)—the frequently observed malignant tumor in the head and neck—develops from oral mucosal squamous epithelial cells and accounts for approximately 90% of oral cancer cases worldwide.[1] OSCC is a lethal and teratogenic disease that severely impairs flavor perception, chewing, swallowing, and pronunciation and leads to facial disfigurement of patients.[2] Despite substantial advances in diagnosis and therapy over the past three decades, oral cancer has a low 5-year survival rate (approximately 60%).[3–5] The primary therapeutic approaches for managing OSCC include surgical intervention, radiotherapy, chemotherapy, or a combination of these options.[6] Cisplatin (CDDP) serves as the first-line chemotherapeutic agent; however, it kills both healthy and cancer cells due to its lack of targeting ability, resulting in severe systemic toxicity, including gastrointestinal toxicity, nephrotoxicity, and hepatotoxicity.[7,8] Moreover, the other obstacle in the clinic is long-term drug resistance during treatment.[9] Therefore, diminishing the toxic side effects, overcoming chemoresistance, and improving the clinical efficacy of chemotherapy drugs are urgent problems that need to be solved.

Nanotechnology advancements hold promise in targeted therapy for OSCC. Nanoparticle (NP)-based drug delivery systems leverage the enhanced permeability and retention (EPR) effect to achieve tumor-selective accumulation, thereby reducing off-target toxicity to healthy tissues.[10–12] For instance, Wei *et al.* developed a nanoliposome platform for co-delivering evodiamine (EVO) and indocyanine green (ICG) in OSCC therapy.[13] Magnetic nanoparticles (MNPs) can be guided to tumor sites and controlled using external magnetic fields, facilitating precise delivery of therapeutic agents.[14,15] Iron oxide nanoparticles, particularly Fe_3O_4 NPs, are among the most commonly used magnetic nanomaterials. Their excellent superparamagnetic characteristics, biodegradability, and biocompatibility make them optimal candidates for biomedical applications.[16,17] The application of Fe_3O_4-based nanocarriers could provide a potential solution to the limitations of platinum-based chemotherapeutic drugs and enhance their therapeutic effects.

More notably, chemoresistance is one of the main causes for the poor prognosis of OSCC patients.[18–20] To overcome drug resistance in cancer treatment, chemotherapy has been integrated with other treatment approaches, namely photothermal therapy (PTT) and photodynamic therapy (PDT), to create a dual-modal synergistic therapy.[21–23] However, oxygen-dependent PDT's therapeutic impact is highly limited

Jiangxi Provincial Key Laboratory of Oral Diseases, Department of Stomatology, The First Affiliated Hospital, Jiangxi Medical College, Nanchang University, Nanchang, Jiangxi, China. E-mail: qiujiaxuan@163.com

† Electronic supplementary information (ESI) available. See DOI: https://doi.org/10.1039/d5ra01910a

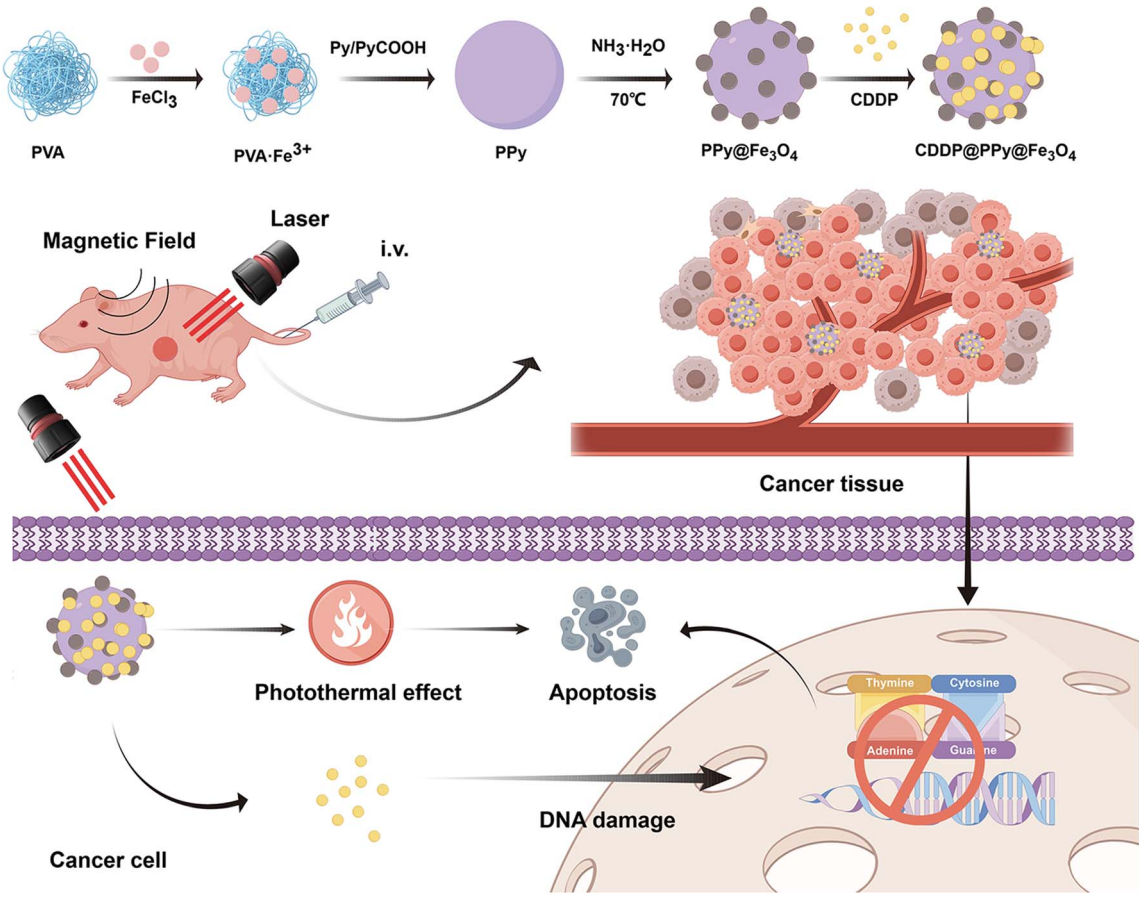

Fig. 1 CDDP@PPy@Fe_3O_4 nanoparticle synthesis along with combined chemo-photothermal therapy in the tumor microenvironment.

considering the intrinsic hypoxic tumor microenvironment.[24–26] PTT is oxygen-independent, non-invasive, and can precisely target tumors compared with existing therapeutic modalities.[27,28] In particular, PTT can not only directly ablate cancer cells through localized heat converted from near-infrared (NIR) light by photothermal transduction agents (PTAs),[29,30] but also improve chemotherapy's efficacy by boosting tumor sensitivity to chemotherapeutic agents.[31] The integration of PTT with chemotherapy is extensively studied and viewed as a promising approach for cancer treatment.[32,33] For example, Song *et al.* designed a nanocarrier system integrating CDDP with chlorin e6 (Ce6), which exhibited notable synergistic effects of phototherapy and chemotherapy in treating head and neck squamous cell carcinoma.[34]

The therapeutic efficacy of PTT is determined by the photothermal conversion efficiency (PCE) of PTAs. Particularly, polypyrrole (PPy) nanoparticles hold promise for biomedical applications considering excellent photostability, high PCE, strong NIR absorption, and ease of fabrication.[35,36] In many cases, the efficiency of photothermal conversion in PPy nanoparticles surpasses that of gold nanorods, which are recognized as well-known photothermal agents.[37] Furthermore, PPy nanomaterials have better biocompatibility compared with inorganic photothermal agents and could be used as a promising PTA for tumor therapy.[38]

In this study, CDDP@PPy@Fe_3O_4 NPs were constructed to integrate chemotherapy and PTT into one nanoplatform for targeted synergistic chemo-photothermal therapy of OSCC (Fig. 1). These NPs assemble in tumor cells *via* the EPR effect, in addition to magnetic guidance. Under NIR laser irradiation, PPy generates localized heat for PTT, enhancing CDDP's efficacy and exerting synergistic anticancer effects. Both cell and animal studies show that CDDP@PPy@Fe_3O_4 NPs significantly enhanced tumor suppression, demonstrating their applicability in clinical scenarios.

2. Materials and methods

2.1 Materials

Pyrrole-1-propanoic acid (Py-COOH), pyrrole (Py), polyvinyl alcohol (PVA), ammonium hydroxide ($NH_3 \cdot H_2O$), cisplatin, and iron(III) chloride hexahydrate ($FeCl_3 \cdot 6H_2O$) were obtained from Aladdin Reagent Co., Ltd (Shanghai, China). Human umbilical vein endothelial cells (HUVEC) and the human OSCC cell line CAL27 were purchased from Anwei Biotechnology Co., Ltd (Shanghai, China). Healthy human oral keratinocytes (HOK) were obtained from Tongpai Biotechnology Co., Ltd (Shanghai, China). The calcein-acetoxymethyl (AM)/propidium iodide (PI) Double Stain Kit, Cell Counting Kit-8 (CCK-8), and cell culture-

related items were sourced from Solarbio Science & Technology Co., Ltd (Beijing, China).

2.2 PPy NP preparation

We dissolved 0.75 g of PVA in 10 mL deionized water (DI) and magnetically mixed at 90 °C for 3 h. Second, we added 373 mg of $FeCl_3$ and vigorously mixed it for 1 h. Third, a monomer mixture of 59.5 mg Py-COOH and 69.2 μL Py was slowly introduced, allowing the reaction to proceed at 4 °C with magnetic stirring for 24 h. Finally, a dark-colored dispersion PPy NP dispersion was obtained.

2.3 PPy@Fe_3O_4 NP preparation

First, 3 mL of the PPy NP dispersion was combined with 18 mL of DI and 2.4 mL of ethanol and mixed for 10 min. Second, we rapidly heated it to 70 °C. Third, we added 1.2 mL of 1 wt% aqueous ammonia to the solution and mixed it for 30 min. Fourth, we added 1.2 mL ammonia solution, followed by stirring for another 30 min at 70 °C. Finally, PPy@Fe_3O_4 NPs were extracted and centrifuged for 50 min at 11 000 rpm, rinsed thrice using DI, and re-suspended in water for subsequent use.

2.4 CDDP@PPy@Fe_3O_4 NP preparation

First, a 10 mL aqueous dispersion of PPy@Fe_3O_4 NPs (4 mg mL^{-1}) was added to 5 mL of CDDP (4 mg mL^{-1} in *N*,*N*-dimethylformamide). The solution was stirred gently in darkness for 72 h. Finally, the reaction mixture was centrifuged to remove excess CDDP, and the CDDP@PPy@Fe_3O_4 was rinsed three times using ultrapure water.

2.5 Characterization

Transmission electron microscopy (TEM; JEOL, JEM-2100F, Japan) examined the sample size and morphology. Chemical structures were evaluated *via* fourier transform infrared (FTIR) spectroscopy (Nicolet iS20, Thermo Fisher Scientific, USA). A Zetasizer Nano ZS90 instrument (Malvern, UK) measured the zeta potential, and a laser particle size analyzer (Bettersize 2600, China) determined the hydrodynamic diameter. An X-ray diffractometer (XRD) (Rigaku SmartLab SE, Japan) conducted the phase analysis. X-ray photoelectron spectroscopy (XPS; Thermo Kalpha, USA) analyzed the chemical state and elemental composition. A vibrating sample magnetometer (VSM; LakeShore 7404, USA) evaluated the magnetic properties. A UV-2600 spectrophotometer (Shimadzu, Japan) recorded the UV-vis absorption spectra. Finally, inductively coupled plasma-optical emission spectrometry (ICP-OES) (Agilent 730, USA) quantified Pt concentrations.

2.6 Photothermal properties

The optical absorption of varying CDDP@PPy@Fe_3O_4 NP concentrations (25, 50, 100, 200, and 400 μg mL^{-1}) was measured using UV-vis spectroscopy. Then, CDDP@PPy@Fe_3O_4 NPs underwent 808 nm NIR irradiation (1 W cm^{-2}) at varying concentrations. Furthermore, 200 μg mL^{-1} of CDDP@PPy@Fe_3O_4 NPs was exposed to different power densities (0.5, 0.75, 1, 1.25, and 1.5 W cm^{-2}). To assess photothermal stability, 200 μg mL^{-1} of CDDP@PPy@Fe_3O_4 was irradiated with an 808 nm laser for 10 min (1 W cm^{-2}). Subsequently, the laser was switched off, cooling the sample for another 10 min. This cycle was repeated five times, and an infrared thermal camera observed variations in temperature. The PCE of CDDP@PPy@Fe_3O_4 NPs was determined based on real-time thermal profiles recorded during laser irradiation.

2.7 Biocompatibility test

To evaluate the biosafety of PPy@Fe_3O_4 nanoparticles, the CCK-8 assay was conducted using HUVEC and HOK cells. First, we incubated cells in 96-well plates at 8000 cells per well density for 24 h. Second, we replaced the medium with a fresh medium comprising PPy@Fe_3O_4 NPs at varying concentrations (0.075, 0.15, 0.3, 0.6, 1.2 and 2.4 mg mL^{-1}), followed by another 24 h of incubation. Five replicate wells were designed for each group. Third, we removed the supernatant and washed the cells two times using PBS. Fourth, we incubated each well with 100 μL of serum-free medium and 10 μL of CCK-8 for another 2 h. Absorbance was recorded at 450 nm using a multifunctional microplate reader. Fifth, we cultured HUVEC cells overnight in 24-well plates at 3×10^4 cells per well density and exposed them to PPy@Fe_3O_4 NPs (0.075, 0.15, 0.3, 0.6, 1.2, and 2.4 mg mL^{-1}) for another 24 h. We stained the cells *via* the Calcein-AM/PI Double Stain Kit for 30 min in a darkroom and visualized them under a fluorescence microscope.

2.8 Drug release performances

The release behavior of CDDP from CDDP@PPy@Fe_3O_4 was evaluated by ICP-OES. Briefly, CDDP@PPy@Fe_3O_4 was suspended in PBS at pH 7.4, with or without 808 nm laser irradiation (1 W cm^{-2}). The mixtures were maintained in a shaking incubator at 37 °C. At predetermined time points, 1 mL aliquots were collected from each group, centrifuged for ultrafiltration, and the Pt concentrations in the supernatants were quantified by ICP-OES.

2.9 *In vitro* anticancer assessment

To evaluate the impact of chemotherapy along with photothermal therapy, the human OSCC cell line CAL27 underwent CCK-8 and calcein-AM/PI double staining. First, we seeded cells to 96-well plates at 8000 cells per well density and incubated them for 24 h. Then the cells were treated with free CDDP, PPy@Fe_3O_4 and CDDP@PPy@Fe_3O_4 at the CDDP concentration of 0.25, 0.5, 1, 2, 4, 8, and 16 μg mL^{-1} (equivalent CDDP and PPy@Fe_3O_4 contents in different groups). Cells treated with PPy@Fe_3O_4 and CDDP@PPy@Fe_3O_4 received an 808 nm laser at 1 W cm^{-2} for 10 min. Finally, the CCK-8 assay examined cell viability. The combination index (CI) was calculated using the Chou-Talalay method in CompuSyn software to evaluate the synergistic effect between chemotherapy and PTT. The IC_{50} value of CDDP was applied to set the concentration of the positive control group in the subsequent CCK-8 assay. Second, we cultured CAL27 cells into 96-well plates and incubated them for 24 h into six groups: control, PPy@Fe_3O_4, PPy@Fe_3O_4 + L (laser), free CDDP, CDDP@PPy@Fe_3O_4, and CDDP@PPy@Fe_3O_4 + L. The groups receiving laser treatment received an 808 nm

laser at 1 W cm^{-2} for 10 min. Following 24 h, we removed the supernatant. Finally, we rinsed the cells two times with PBS. The cell survival rate was determined through CCK-8 absorbance measurements after 2 h of incubation.

For the calcein-AM/PI staining assay, we cultured CAL27 cells in 24-well plates at 8×10^4 cells per well density and incubated them overnight. They were separated into six groups, as mentioned earlier. For 10 min, laser-treated groups received an 808 nm laser at 1 W cm^{-2}. Following another 24 h, cells were stained with calcein-AM/PI and captured under a fluorescence microscope.

2.10 *In vivo* anticancer assessment

A BALB/c nude mouse model of OSCC was developed by subcutaneously injecting 4×10^6 CAL27 cells (100 μL) into the right flank. Tumor growth was assessed by calculating the longest (L) and shortest (S) diameters on alternate days, with the tumor volume calculated as: $V = (L \times S^2)/2$. Once tumors reached approximately 100 mm^3, the animals were categorized as follows: (i) control (PBS), (ii) free CDDP, (iii) CDDP@PPy@Fe_3O_4, (iv) PPy@Fe_3O_4 + L, (v) CDDP@PPy@Fe_3O_4 + L, and (vi) CDDP@PPy@Fe_3O_4 + M (magnet) + L. Each group contained five mice. The groups were intravenously injected with corresponding samples only once, with 5 mg kg^{-1} CDDP administered (equivalent CDDP content in different samples). Day 0 was designated as the injection day. The mice of group 6 were exposed to a small magnet (0.2 T) attached next to the tumor for 2 h. Twenty-four hours after injection, mice in groups 4, 5, and 6 were exposed to an 808 nm laser at 1 W cm^{-2} for 10 min. A thermal imaging camera monitored temperature and thermal changes. We measured the body weight along with the tumor size every alternate day until day 28. At the experiment's end, the animals were humanely killed, with the tumor removed and weighed. Moreover, the liver, heart, lung, spleen, and kidneys were obtained and fixed for histopathological examination. Animal experiments adhered to Nanchang University's "Laboratory Animal Care and Use Guidelines" and obtained approval from the Animal Ethics Committee (approval number 202401QR013).

2.11 Data analysis

The mean ± standard deviation presents experimental data. A one-way analysis of variance examined significant variations among groups. The Bonferroni test allowed for post hoc analysis. *P*-values < 0.05 suggested statistical significance.

3. Results and discussion

3.1 Synthesis and characterization

CDDP@PPy@Fe_3O_4 synthesis is shown in Fig. 1. Specifically, PPy NPs were prepared *via* aqueous dispersion polymerization,

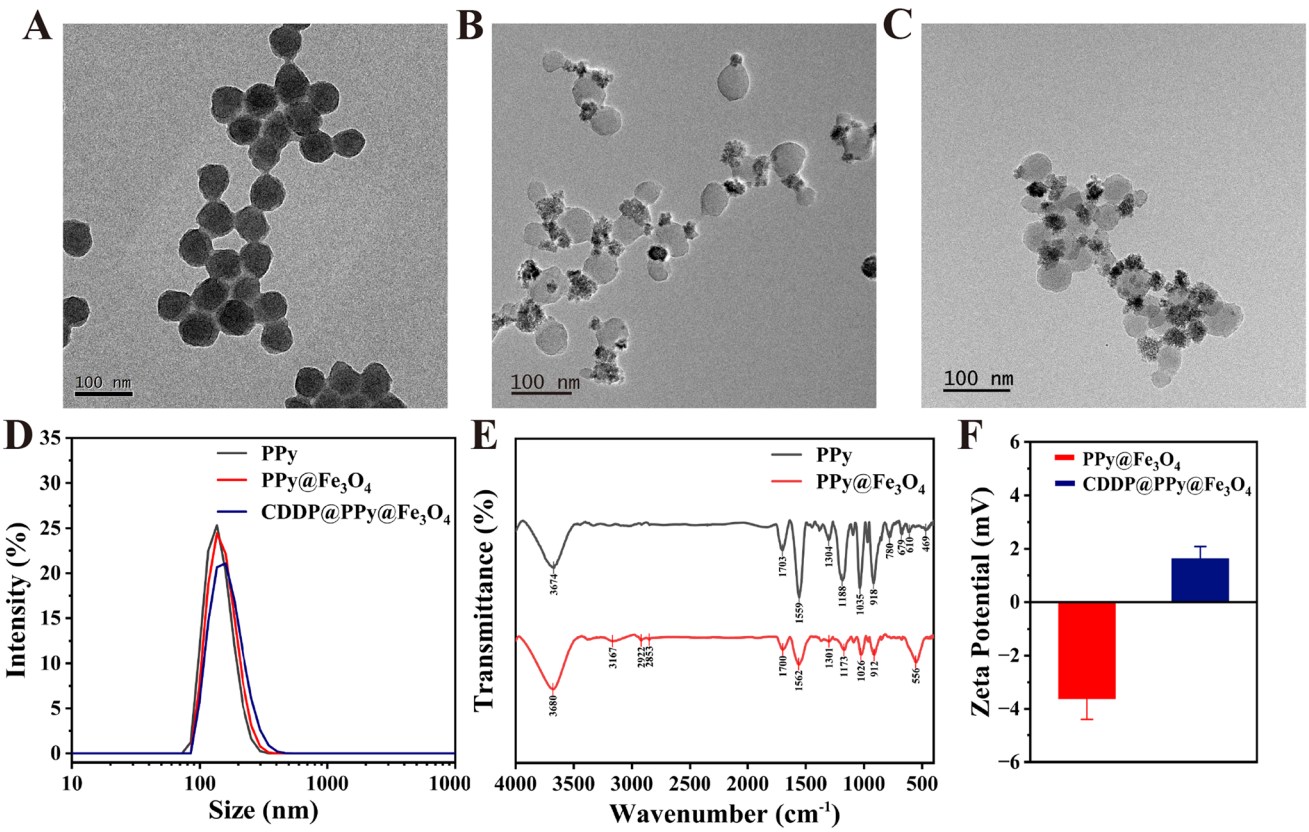

Fig. 2 (A–C) Transmission electron microscopy images showing (A) PPy, (B) PPy@Fe_3O_4, and (C) CDDP@PPy@Fe_3O_4. (D) Particle-size distribution of PPy, PPy@Fe_3O_4, and CDDP@PPy@Fe_3O_4. (E) Fourier transform infrared spectroscopy of PPy and PPy@Fe_3O_4. (F) Zeta potential of PPy@Fe_3O_4 and CDDP@PPy@Fe_3O_4.

using $FeCl_3$ as an oxidizing agent, whereas PVA served as a capping agent controlling particle size and improving hydrophilicity. Py and Py-COOH were mixed with the PVA/Fe^{3+} aqueous solution to form PPy NPs with carboxyl groups. Subsequently, on PPy NP surfaces, reduced Fe^{2+} ions and unreacted Fe^{3+} ions formed magnetic iron oxide nanocrystals *in situ* by adding ammonia while it was heated to 70 °C, creating PPy@Fe_3O_4 NPs. Next, CDDP was reacted with PPy@Fe_3O_4 NP surface carboxyl, yielding CDDP@PPy@Fe_3O_4 NPs. TEM images showed the size and morphology of PPy, PPy@Fe_3O_4 and CDDP@PPy@Fe_3O_4 NPs (Fig. 2A–C), which have average diameters of 143.9 nm, 153.7 nm and 167.3 nm respectively according to the measurements of DLS (Fig. 2D). The FTIR spectrum was used to further analysis the chemical structure of the nanocomposite, with the results depicted in Fig. 2E. The appearance of new bands at 556 cm^{-1} suggested Fe–O stretching vibrations. Therefore, PPy@Fe_3O_4 was successfully formed. The HAADF-STEM image of PPy@Fe_3O_4 nanocomposite, along with its elemental mapping, revealed elemental C, N, Fe, and O distributions (Fig. S1†). In addition, the altered zeta potential confirmed effective cisplatin loading (Fig. 2F). Furthermore, the XRD pattern of PPy@Fe_3O_4 (Fig. 3A) exhibited peaks corresponding to Fe_3O_4 nanocrystals (JCPDS No. 65-3107). Since the XRD patterns of Fe_3O_4 and γ-Fe_2O_3 are very similar, XPS analyzed Fe chemical states, confirming the presence of both Fe^{2+} and Fe^{3+} ions in the iron oxide, and the formation of Fe_3O_4 within the nanocomposite was verified (Fig. 3B). Meanwhile, the XPS data of CDDP@PPy@Fe_3O_4 presented the appearance of Pt 4f compared with that of PPy@Fe_3O_4, confirming successful loading of cisplatin (Fig. 3C). The findings above coherently demonstrated the successful synthesis of CDDP@PPy@Fe_3O_4 nanocomposite. ICP-OES and thermogravimetric analysis (TGA) were performed to determine the composition of the nanocomposite. The results revealed that CDDP and Fe_3O_4 accounted for 6.8% and 43.6% by weight, respectively (Fig. S2†). Moreover, the magnetization measurement indicated that CDDP@PPy@Fe_3O_4 NPs had excellent superparamagnetism with 40.7 emu g^{-1} saturation magnetization at room temperature (Fig. 3D), which provided the magnetic targeting function for the NPs.

3.2 Photothermal effects

As shown in Fig. S3,† the aqueous dispersions of PPy@Fe_3O_4 and CDDP@PPy@Fe_3O_4 NPs with different concentrations showed strong and widespread absorption across the near-infrared and visible regions, indicating their potential for photothermal therapy. To evaluate the photothermal properties, samples containing different concentrations of CDDP@PPy@Fe_3O_4 NPs received an 808 nm laser at 1 W cm^{-2}

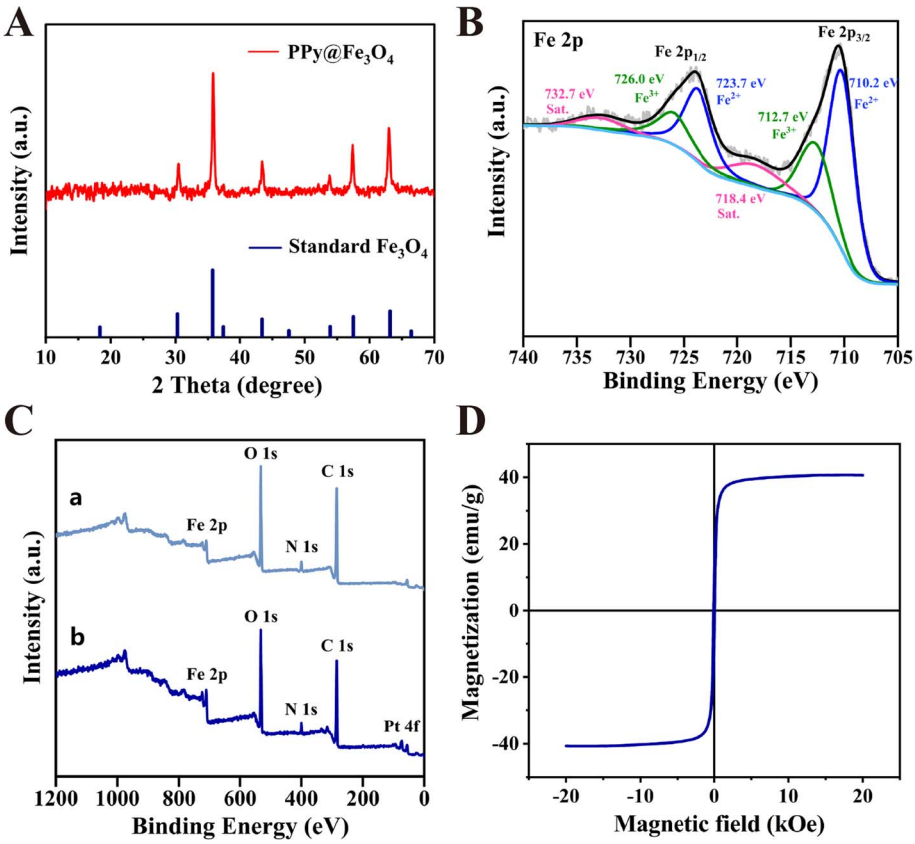

Fig. 3 (A) X-ray diffraction pattern showing PPy@Fe_3O_4. The standard Fe_3O_4 (JCPDS No. 65-3107) pattern is provided at the bottom for reference. (B) High-resolution X-ray photoelectron spectroscopy (XPS) spectrum of the Fe 2p region. (C) Comparative XPS spectra of (a) PPy@Fe_3O_4 and (b) CDDP@PPy@Fe_3O_4 in the wide-scan range. (D) Room-temperature magnetic hysteresis loop of CDDP@PPy@Fe_3O_4.

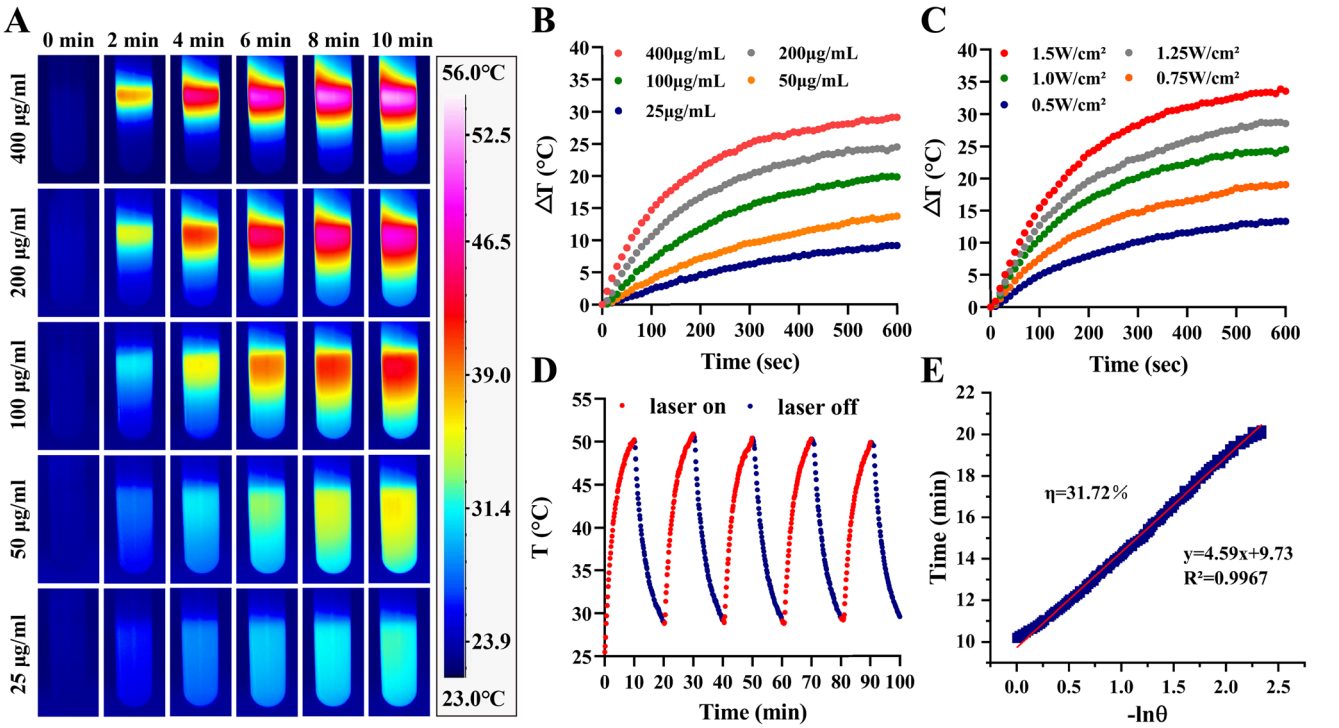

Fig. 4 Photothermal properties of CDDP@PPy@Fe_3O_4 nanoparticles (NPs). (A) Thermographic images and (B) corresponding heating curves of varying CDDP@PPy@Fe_3O_4 NP concentrations (808 nm, 1 W cm^{-2}). (C) Heating curves of 200 μg mL^{-1} CDDP@PPy@Fe_3O_4 NPs under varying power densities. (D) Heating-cooling curves of 200 μg mL^{-1} CDDP@PPy@Fe_3O_4 NPs under repeated cycles at 1 W cm^{-2}. (E) Calculation of photothermal conversion efficiency (PCE).

for 10 min (Fig. 4B), while using an infrared camera to capture temperature variations in real-time (Fig. 4A). The temperature rose in a concentration-dependent manner and increased >29 °C upon reaching 400 μg mL^{-1}, indicating that CDDP@PPy@Fe_3O_4 NPs are capable of efficiently generating thermal energy from an 808 nm NIR light. As depicted in Fig. 4C, under varying laser power densities, heating curves of 200 μg mL^{-1} CDDP@PPy@Fe_3O_4 NPs affirmed that the photothermal effect was correlated with the power density of the irradiation source. Subsequently, the temperature profiles for heating and cooling for 200 μg mL^{-1} CDDP@PPy@Fe_3O_4 NPs were monitored at 1 W cm^{-2} (Fig. 4D). Significant variation in temperature elevation was not detected over five uninterrupted laser on/off cycles, indicating higher photostability of CDDP@PPy@Fe_3O_4 NPs. The PCE of CDDP@PPy@Fe_3O_4 was calculated as 31.72% (Fig. 4E), surpassing the 25% PCE reported for the gold nanorod-based nanocomposite.[39] In summary, the commendable photothermal characteristics of CDDP@PPy@Fe_3O_4 NPs, encompassing efficient photothermal conversion performance and remarkable photostability, render them highly suitable for PTT.

3.3 Biocompatibility evaluation

Biocompatibility is a key determinant in biomaterial design for anticancer therapies.[40] The cytotoxicity of PPy@Fe_3O_4 NPs at various concentrations on HUVEC and HOK cells was assessed *via* calcein-AM/PI co-staining along with the CCK-8 assay. Based on the CCK-8 findings, differences in cell viability with and without PPy@Fe_3O_4 NPs co-incubation were not observed (Fig. 5A and B). Consistent with the above results, calcein-AM/PI staining confirmed that treatment with PPy@Fe_3O_4 NPs did not cause any significant harm to HUVEC cells, even after exposing the cells to as far as 2.4 mg mL^{-1} NPs for 24 h (Fig. 5C). These findings indicate that the prepared carrier itself is featured with high biocompatibility and safety.

3.4 *In vitro* anticancer effects

The drug release profiles of CDDP from CDDP@PPy@Fe_3O_4 are shown in Fig. 6A. In the absence of NIR irradiation, CDDP@PPy@Fe_3O_4 released approximately 48.1% of CDDP within 24 h. Under NIR irradiation, the cumulative release increased to 53.6%. This enhancement is attributed to the photothermal effect of PPy, which converts NIR light into thermal energy, inducing localized heating that facilitates the dissociation of coordination bonds.[41]

The therapeutic efficacy of single therapy and combination therapy were evaluated by CCK-8 assay. As shown in Fig. 6B, CDDP@PPy@Fe_3O_4 under NIR laser irradiation exhibits stronger cell-killing effects than both free CDDP (without irradiation) and PPy@Fe_3O_4 under identical NIR irradiation conditions. The data were analyzed using CompuSyn software.[42,43] As presented in Fig. S4,† the CI was <1, indicating that CDDP@PPy@Fe_3O_4 NPs under NIR irradiation demonstrated a synergistic anticancer effect between chemotherapy and PTT.

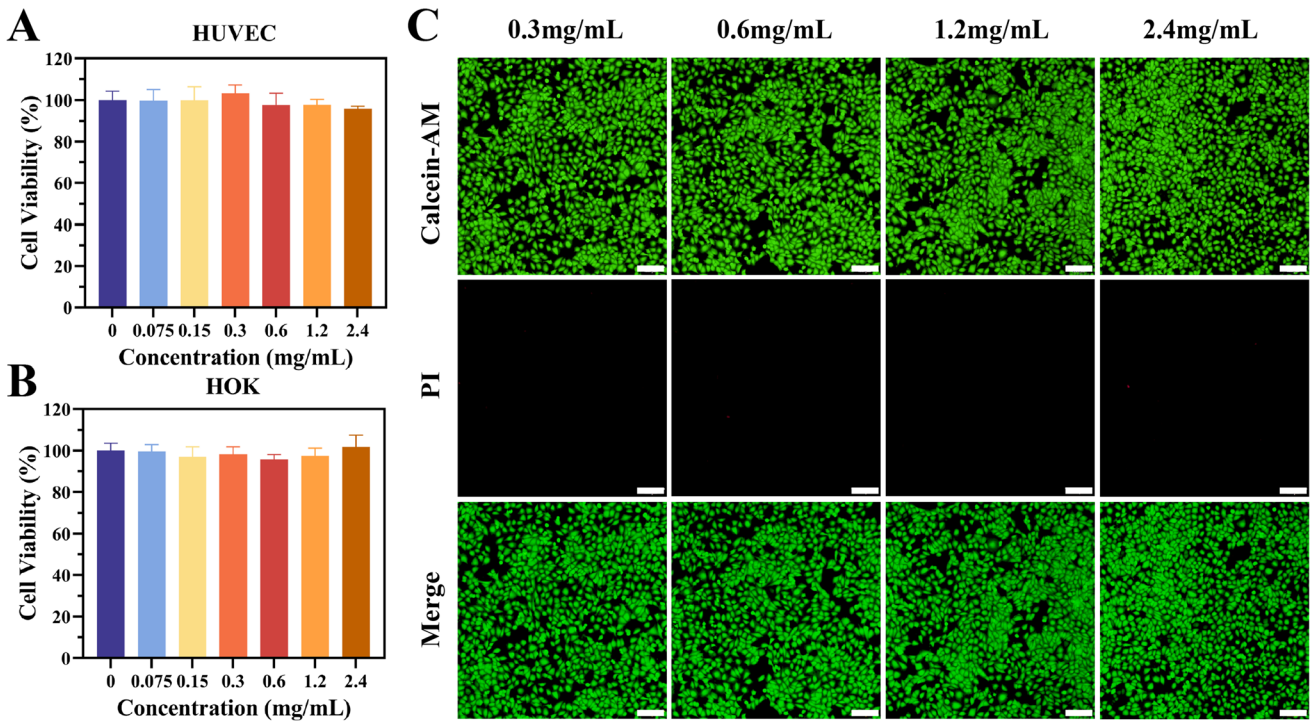

Fig. 5 PPy@Fe_3O_4 NP cytotoxicity (A and B) Cell Counting Kit-8 assay results showing human umbilical vein endothelial cells (HUVEC) and human oral keratinocytes survival rates after exposure to varying PPy@Fe_3O_4 NPs concentrations for 24 h. (C) Calcein-acetoxymethyl/propidium iodide staining showing fluorescent HUVEC. Scale bar: 200 μm.

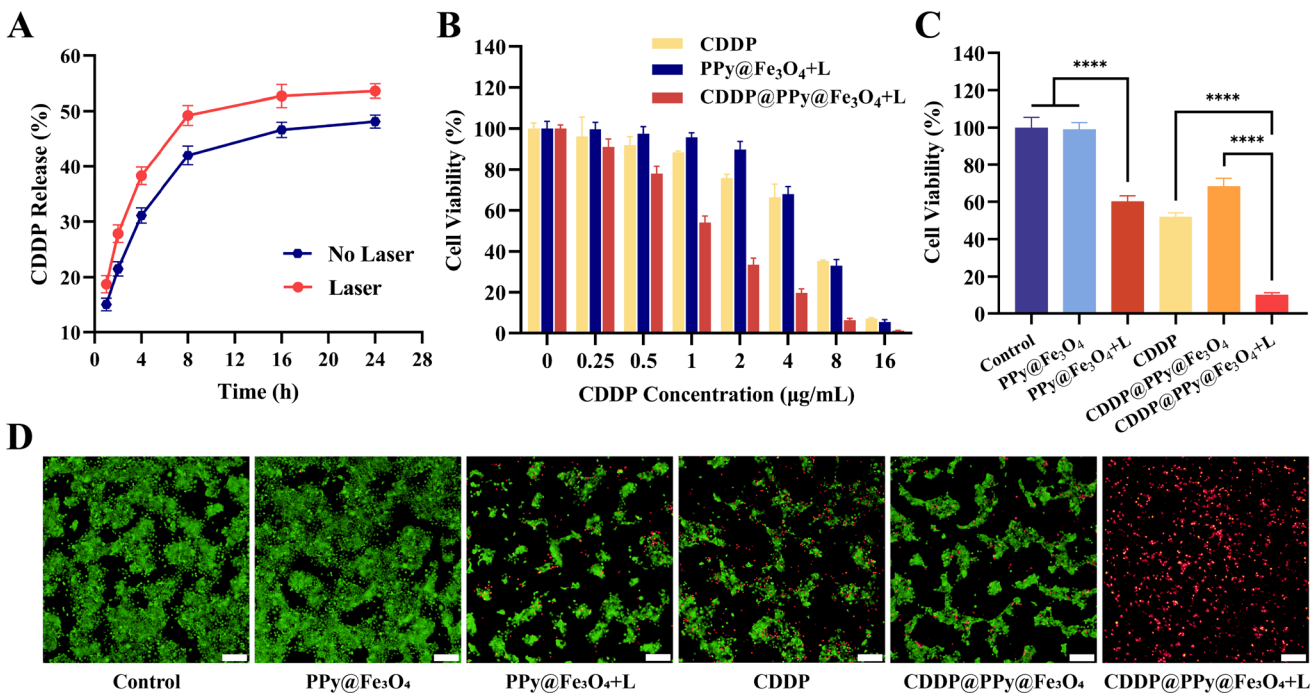

Fig. 6 *In vitro* release and anticancer effect. (A) Cumulative release of CDDP from CDDP@PPy@Fe_3O_4. (B and C) CAL27 cell viability after treatment, receiving or not receiving an 808 nm laser for 10 min at 1 W cm^{-2}. (D) Calcein-acetoxymethyl/propidium iodide staining showing fluorescent CAL27 cells. Scale bar: 200 μm. (L: laser).

Fig. S5† illustrates that the IC_{50} value of CDDP in CAL27 cells was 5.1 μg mL^{-1}. Then, cells were classified into six groups: control, PPy@Fe_3O_4, PPy@Fe_3O_4 + L, free CDDP, CDDP@PPy@Fe_3O_4, and CDDP@PPy@Fe_3O_4 + L. (CDDP: 5.1 μg mL^{-1}, PPy@Fe_3O_4: 69.9 μg mL^{-1}, and CDDP@PPy@Fe_3O_4: 75 μg mL^{-1}). PPy@Fe_3O_4 NPs treatment resulted in a cell viability

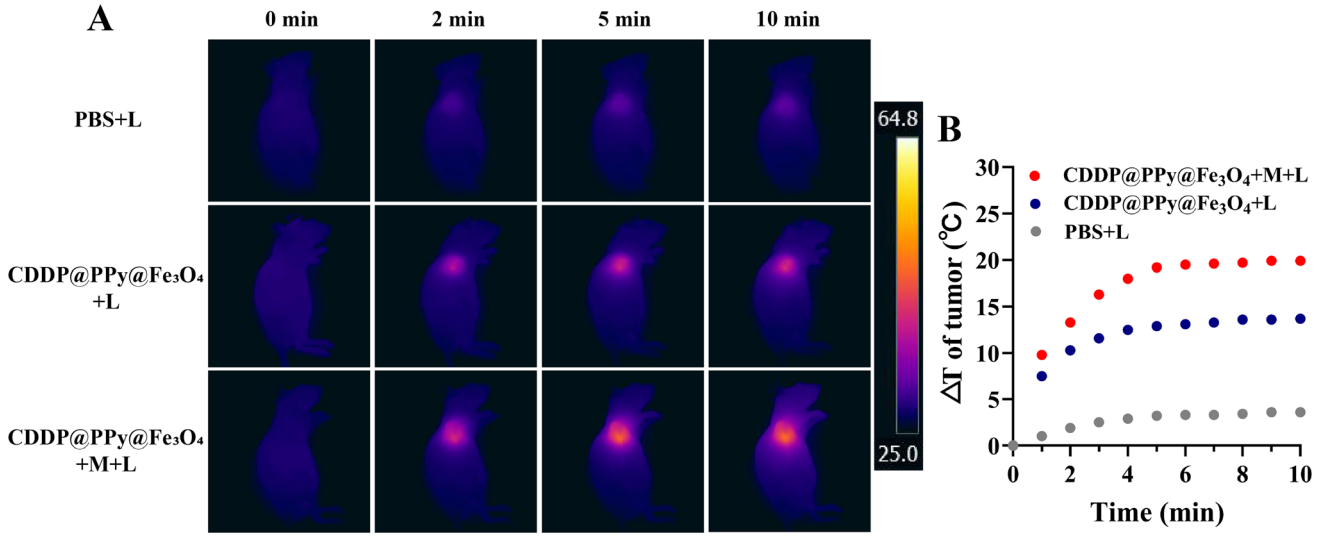

Fig. 7 *In vivo* photothermal properties of CDDP@PPy@Fe_3O_4 nanoparticles. (A) Infrared thermographic images of tumor-bearing mice (CAL27 xenografts) receiving an 808 nm laser for 10 min at 1 W cm^{-2}. (B) Corresponding temperature profiles. (L: laser; M: magnet).

of 60% with 808 nm laser irradiation and 99% without laser irradiation (Fig. 6C). This observation suggests that the photothermal effect is capable of directly killing cancer cells. Furthermore, post-treatment with free CDDP, 52% of CAL27 cells remained viable, in contrast to only 10% cell survival observed following treatment with CDDP@PPy@Fe_3O_4 NPs under 808 nm laser irradiation. Additionally, the calcein-AM/PI co-staining assay indicated the synergistic therapeutic effects (Fig. 6D). The control and PPy@Fe_3O_4 NPs groups exhibited minimal red fluorescence. While treated with free CDDP, CDDP@PPy@Fe_3O_4 NPs alone or PPy@Fe_3O_4 NPs coupled with laser irritation, only partial cells underwent apoptosis, respectively. However, significant cancer cell death occurred upon treatment with CDDP@PPy@Fe_3O_4 NPs followed by NIR laser irradiation, aligning with CCK-8 assay results. The above results collectively demonstrate that CDDP@PPy@Fe_3O_4 NPs can integrate chemotherapy and photothermal therapy, yielding remarkable therapeutic effects on cancer cells.

3.5 *In vivo* anticancer effects

Building upon the *in vitro* photothermal performance and outstanding chemo-photothermal synergistic therapeutic efficacy of CDDP@PPy@Fe_3O_4 NPs, CAL27 xenograft tumor-bearing mice allowed for examining the anticancer potential *in vivo*. Random assignment divided the animals into six groups, each subjected to a distinct treatment regimen. The infrared thermography camera captured images of tumor site temperature variations at various time points. As displayed in Fig. 7A and B, the PBS-treated group exhibited a temperate increase by only 3.6 °C during irradiation. On the contrary, local temperature changes in irradiated tumors of the CDDP@PPy@Fe_3O_4 + L and CDDP@PPy@Fe_3O_4 + M + L groups reached 13.7 °C and 19.9 °C, respectively, after 10 min of NIR exposure, which were sufficient for hyperthermia or thermal ablation of tumor tissue.[44] Meanwhile, these findings demonstrated the effective accumulation of the NPs in the tumor, particularly when guided by a magnetic field. Fig. 8A illustrates the treatment process of mice with CAL27 tumors. Variations in the tumor size across each experimental condition are shown in Fig. 8B. Significantly elevated tumor volumes were found in the PBS group over 28 days. Compared with the group receiving free CDDP, the CDDP@PPy@Fe_3O_4 + M + L group demonstrated a more pronounced efficacy in suppressing tumor growth, resulting from photothermal therapy along with chemotherapy, intensified by the magnetic targeting capabilities of the CDDP@PPy@Fe_3O_4 NPs. Besides, these superior tumor-suppressing outcomes were corroborated by measuring the weights of excised tumors across different experimental groups and by assessing their corresponding photographs (Fig. 8D and E). Throughout the 28-day experiment, no significant weight fluctuations were observed (Fig. 8C), suggesting that CDDP@PPy@Fe_3O_4 NPs in addition to NIR did not result in pronounced systemic toxicity. Besides, the typical histopathological damage in addition to nuclear condensation of tumor cells (Fig. 8F) and significant inhibition of tumor cell proliferative capacity (Fig. 8G) were obviously displayed in the CDDP@PPy@Fe_3O_4 + M + L group compared with the groups of PBS and free CDDP, which was consistent with the therapeutic results described above. Meanwhile, histological analysis using hematoxylin and eosin staining did not reveal damaged tissue in major organs (Fig. S6†), suggesting that the CDDP@PPy@Fe_3O_4 NPs had excellent biosafety *in vivo*. All the abovementioned therapeutic outcomes demonstrated that CDDP@PPy@Fe_3O_4 NPs possessed desirable biosafety and enhanced therapeutic efficacy when subjected to a magnetic field and NIR laser radiation.

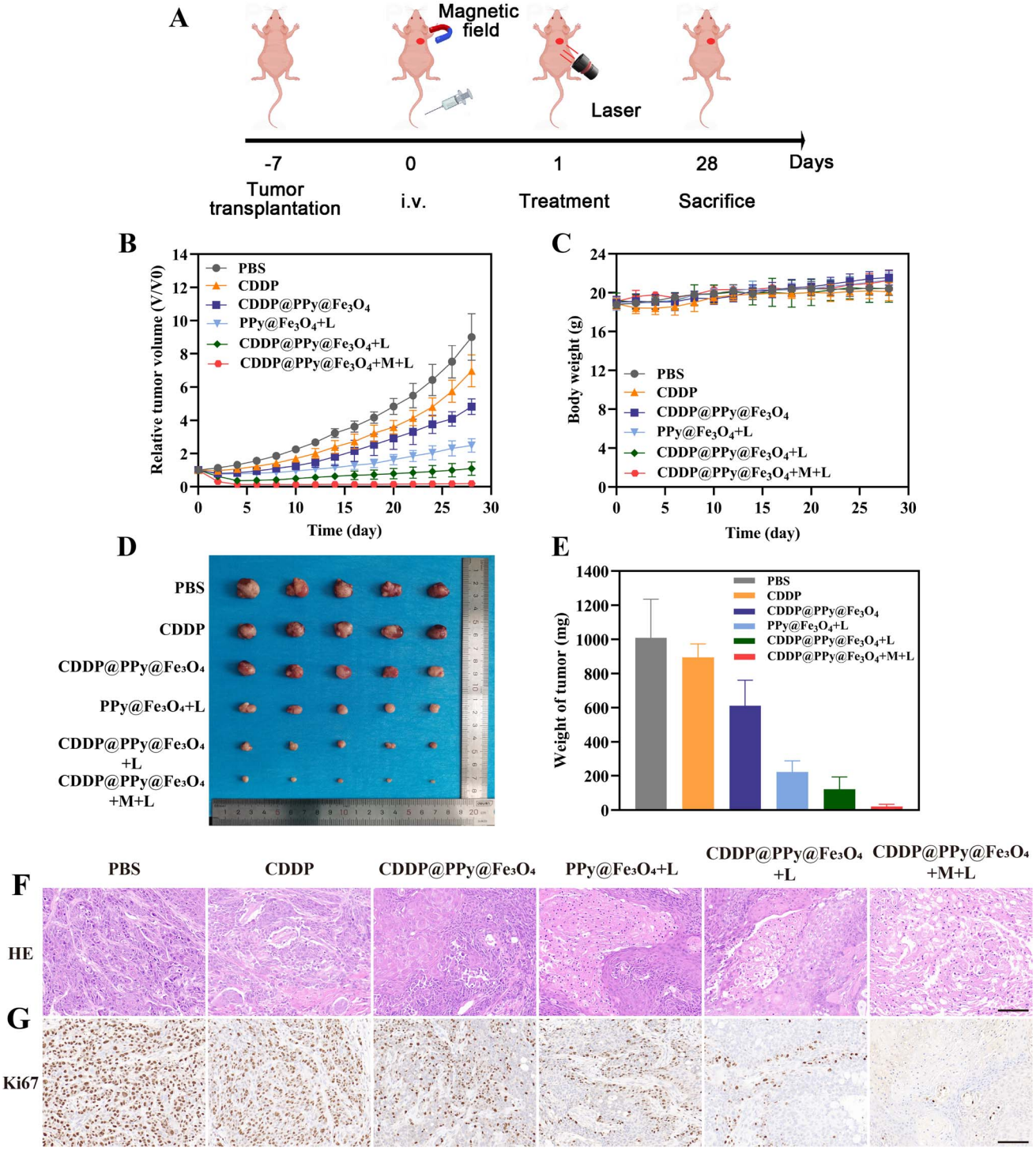

Fig. 8 Tumor suppression efficacy of CDDP@PPy@Fe_3O_4 nanoparticles in CAL27 tumor-bearing mice. (A) Treatment process. Changes in (B) tumor volume and (C) nude mice body weight in diverse experimental conditions. (D) Images and (E) excised tumor weights on day 28. (F) Hematoxylin and eosin and (G) Ki-67 antigen staining showing excised tumors from different experimental groups. Scale bar: 100 μm. (L: laser; M: magnet).

4. Conclusions

In conclusion, this study successfully developed a CDDP@PPy@Fe_3O_4 nanocomposite for synergistic chemo-photothermal therapy targeting OSCC. This chemotherapeutic nanomedicine functions not only as a nanocarrier for the delivery of CDDP but also demonstrates exceptional PCE and photostability, thus enabling its use for hyperthermia and photothermal ablation of tumors. Furthermore, CDDP@PPy@Fe_3O_4 NPs promote increased drug accumulation within tumors *via* the

EPR effect and magnetic field guidance, thereby reducing the systemic toxicity typically associated with chemotherapy. As expected, upon exposure to NIR light, CDDP@PPy@Fe_3O_4 NPs significantly inhibited tumors both *in vivo* and *in vitro*. Taken together, the developed CDDP@PPy@Fe_3O_4 nanocomposite present a promising approach for future synergistic treatment of OSCC.

Currently, immunotherapy has emerged as an attractive therapeutic strategy for cancer treatment.[45] However, the clinical response rate of immunotherapy alone remains limited. The combination of chemotherapy and immunotherapy may overcome the limitations of monotherapy.[46] Additionally, previous studies reported that the photothermal effect can not only directly kill tumor cells but also induce immunogenic cell death, releasing tumor antigens and damage-associated molecular patterns, thereby activating antitumor immune responses.[47,48] These findings provide us with an idea that CDDP@PPy@Fe_3O_4 could be utilized in combined therapy integrating chemotherapy, PTT and immunotherapy. Future studies will focus on systematically exploring the synergistic interactions between CDDP@PPy@Fe_3O_4 and other therapeutic modalities.

Data availability

All data supporting the findings of this study are included within the manuscript.

Author contributions

Danrui Liu: methodology, investigation, data curation, formal analysis, visualization, and writing – original draft. Wenquan Wang: methodology, data curation, formal analysis, and visualization. Yongjun Li: data curation, validation, and visualization. Suai Lin: formal analysis and validation. Qingkun Jiang: formal analysis and validation. Ruiyang Zou: investigation. Jiaxuan Qiu: conceptualization, supervision, funding acquisition, and writing – review and editing.

Conflicts of interest

There are no conflicts to disclose.

Acknowledgements

This work was supported by the National Natural Science Foundation of China (No. 82260194, 82403716), the Jiangxi Natural Science Foundation (No. 20232BAB216073, 20242BAB25514), and the Key Projects of the Jiangxi Administration of Traditional Chinese Medicine (No. GZY-KJS-2023-028).

Notes and references

1 A. W. Y. Chai, K. P. Lim and S. C. Cheong, *Semin. Cancer Biol.*, 2020, **61**, 71–83.
2 Y. Tan, Z. Wang, M. Xu, B. Li, Z. Huang, S. Qin, E. C. Nice, J. Tang and C. Huang, *Int. J. Oral Sci.*, 2023, **15**, 44.
3 R. L. Siegel, K. D. Miller, H. E. Fuchs and A. Jemal, *CA Cancer J. Clin.*, 2022, **72**, 7–33.
4 A. Chamoli, A. S. Gosavi, U. P. Shirwadkar, K. V. Wangdale, S. K. Behera, N. K. Kurrey, K. Kalia and A. Mandoli, *Oral Oncol.*, 2021, **121**, 105451.
5 A. Almangush, A. A. Mäkitie, A. Triantafyllou, R. de Bree, P. Strojan, A. Rinaldo, J. C. Hernandez-Prera, C. Suárez, L. P. Kowalski, A. Ferlito and I. Leivo, *Oral Oncol.*, 2020, **107**, 104799.
6 D. K. Zanoni, P. H. Montero, J. C. Migliacci, J. P. Shah, R. J. Wong, I. Ganly and S. G. Patel, *Oral Oncol.*, 2019, **90**, 115–121.
7 J. Yang, T. Su, H. Zou, G. Yang, J. Ding and X. Chen, *Angew. Chem.*, 2022, **61**, e202211136.
8 S. Song, X. Xia, J. Qi, X. Hu, Q. Chen, J. Liu, N. Ji and H. Zhao, *Drug. Deliv.*, 2021, **28**, 2480–2494.
9 B. Zhao, X. Qin, R. Fu, M. Yang, X. Hu, S. Zhao, Y. Cui, Q. Guo and W. Zhou, *J. Control. Release*, 2024, **368**, 623–636.
10 M. Overchuk and G. Zheng, *Biomaterials*, 2018, **156**, 217–237.
11 Y. Shi, R. van der Meel, X. Chen and T. Lammers, *Theranostics*, 2020, **10**, 7921–7924.
12 R. Sun, J. Xiang, Q. Zhou, Y. Piao, J. Tang, S. Shao, Z. Zhou, Y. H. Bae and Y. Shen, *Adv. Drug Delivery Rev.*, 2022, **191**, 114614.
13 Z. Wei, H. Zou, G. Liu, C. Song, C. Tang, S. Chen, G. Zhang, J. Ran, Y. Wang, X. Yin, Y. Cai and W. Han, *Bioact. Mater.*, 2021, **6**, 2144–2157.
14 A. Farzin, S. A. Etesami, J. Quint, A. Memic and A. Tamayol, *Adv. Healthcare Mater.*, 2020, **9**, e1901058.
15 R. Qiao, C. Fu, H. Forgham, I. Javed, X. Huang, J. Zhu, A. K. Whittaker and T. P. Davis, *Adv. Drug Delivery Rev.*, 2023, **197**, 114822.
16 S. Zhao, X. Yu, Y. Qian, W. Chen and J. Shen, *Theranostics*, 2020, **10**, 6278–6309.
17 W. Sun, X. Chai, Y. Zhang, T. Yu, Y. Wang, W. Zhao, Y. Liu, D. Yin and C. Zhang, *Chem. Rec.*, 2024, **24**, e202400179.
18 S. Wu, X. Lv, H. Wei, W. Chen, J. Zheng, X. Li, J. Song, Y. Ai and C. Zou, *J. Cell. Mol. Med.*, 2023, **27**, 4133–4144.
19 Z. Zhou, S. Han, J. Liao, R. Wang, X. Yu and M. Li, *Am. J. Chin. Med.*, 2023, **51**, 2221–2241.
20 Y. Lugones, P. Loren and L. A. Salazar, *Biomolecules*, 2022, 12.
21 M. Overchuk, R. A. Weersink, B. C. Wilson and G. Zheng, *ACS Nano*, 2023, **17**, 7979–8003.
22 B. Q. Spring, I. Rizvi, N. Xu and T. Hasan, *Photochem. Photobiol. Sci.*, 2015, **14**, 1476–1491.
23 H. Gao, Y. Bai, L. Chen, G. E. Fakhri and M. Wang, *Int. J. Nanomed.*, 2020, **15**, 809–819.
24 S. Li, K. Lin, P. Hu, S. Wang, S. Zhao, Y. Gan, L. Liu, S. Yu and J. Shi, *Int. J. Pharm.*, 2022, **611**, 121307.
25 D. Chen, Q. Xu, W. Wang, J. Shao, W. Huang and X. Dong, *Small*, 2021, **17**, e2006742.
26 H. Zhang, Y. Zhang, Y. Zhang, H. Li, M. Ou, Y. Yu, F. Zhang, H. Yin, Z. Mao and L. Mei, *Nat. Commun.*, 2024, **15**, 6783.
27 Z. Xie, T. Fan, J. An, W. Choi, Y. Duo, Y. Ge, B. Zhang, G. Nie, N. Xie, T. Zheng, Y. Chen, H. Zhang and J. S. Kim, *Chem. Soc. Rev.*, 2020, **49**, 8065–8087.

28 Y. Liu, P. Bhattarai, Z. Dai and X. Chen, *Chem. Soc. Rev.*, 2019, **48**, 2053–2108.
29 L. Zhang, Y. Zhang, Y. Xue, Y. Wu, Q. Wang, L. Xue, Z. Su and C. Zhang, *Adv. Mater.*, 2019, **31**, e1805936.
30 J. Chen, C. Ning, Z. Zhou, P. Yu, Y. Zhu, G. Tan and C. Mao, *Prog. Mater. Sci.*, 2019, **99**, 1–26.
31 D. Tang, H. Zhou, M. Cui, G. Liang, H. Zhang and H. Xiao, *Adv. Mater.*, 2023, **35**, e2300048.
32 D. Zhi, T. Yang, J. O'Hagan, S. Zhang and R. F. Donnelly, *J. Control. Release*, 2020, **325**, 52–71.
33 Y. Wang, L. Chang, H. Gao, C. Yu, Y. Gao and Q. Peng, *Eur. J. Med. Chem.*, 2024, **272**, 116508.
34 C. Song, C. Tang, W. Xu, J. Ran, Z. Wei, Y. Wang, H. Zou, W. Cheng, Y. Cai and W. Han, *Int. J. Nanomed.*, 2020, **15**, 347–361.
35 H. Geng, E. J. Lupton, Y. Ma, R. Sun, C. L. Grigsby, G. Brachi, X. Li, K. Zhou, D. J. Stuckey and M. M. Stevens, *Adv. Healthcare Mater.*, 2023, **12**, e2301148.
36 S. Wang, Z. Ma, Z. Shi, Y. Huang, T. Chen, L. Hou, T. Jiang and F. Yang, *Drug delivery*, 2022, **29**, 1312–1325.
37 Z. Zha, X. Yue, Q. Ren and Z. Dai, *Adv. Mater.*, 2013, **25**, 777–782.
38 W. Huang, T. Leng, M. Gao, Q. Hu, L. Liu and H. Dou, *Carbohydr. Polym.*, 2020, **241**, 116224.
39 R. A. Mustafa, M. Ran, Y. Wang, J. Yan, Y. Zhang, J. M. Rosenholm and H. Zhang, *Smart Mater. Med.*, 2023, **4**, 199–211.
40 C. Liu, T. Zhang, L. Chen and Y. Chen, *Cancer Lett.*, 2020, **487**, 45–52.
41 P. Štarha, D. Smola, J. Tuček and Z. Trávníček, *Int. J. Mol. Sci.*, 2015, **16**, 2034–2051.
42 H. H. Chen, I. L. Lu, T. I. Liu, Y. C. Tsai, W. H. Chiang, S. C. Lin and H. C. Chiu, *Colloids Surf., B*, 2019, **177**, 294–305.
43 X. Yin, S. Ran, H. Cheng, M. Zhang, W. Sun, Y. Wan, C. Shao and Z. Zhu, *Colloids Surf., B*, 2022, **216**, 112507.
44 X. Huang, Y. Lu, M. Guo, S. Du and N. Han, *Theranostics*, 2021, **11**, 7546–7569.
45 Y. Yu, T. Li, M. Ou, R. Luo, H. Chen, H. Ren, Z. Li, J. Sun, H. Zhang, S. Peng, Y. Zhao and L. Mei, *J. Control. Release.*, 2024, **365**, 469–479.
46 Y. Yu, Q. Cheng, X. Ji, H. Chen, W. Zeng, X. Zeng, Y. Zhao and L. Mei, *Sci. Adv.*, 2022, **8**, eadd3599.
47 Y. Zhang, X. Yu, L. Luo, Y. Xu, H. Zhang, Z. Mao, Y. Zhang, C. Yang, L. Wang, P. Zhang, S. Li, M. Ou, R. Luo, D. Zhu, W. Li and L. Mei, *J. Control. Release.*, 2024, **376**, 1115–1129.
48 S. Sheng, X. Yu, G. Xing, L. Jin, Y. Zhang, D. Zhu, X. Dong, L. Mei and F. Lv, *Adv. Funct. Mater.*, 2023, **33**, 2212118.